Lab on a Chip

Contactless, programmable acoustofluidic manipulation of objects on water

Journal:	*Lab on a Chip*
Manuscript ID	LC-ART-05-2019-000465.R1
Article Type:	Paper
Date Submitted by the Author:	15-Aug-2019
Complete List of Authors:	Zhang, Steven Peiran; Duke University, Mechanical Engineering and Materials Science Chen, Chuyi; Duke University, Mechanical Engineering and Materials Science Guo, Feng; indiana university bloomington , Intelligent Systems Engineering Philippe, Julien; Duke University, Center for Human Disease Modeling Gu, Yuyang; Duke University, MEMS Tian, Zhenhua; Duke University, Mechanical Engineering and Materials Science Bachman, Hunter; Duke University, MEMS Ren, Liqiang; The Penn state University, Department of Engineering Science and Mechanics Yang, Shujie; Duke University, Mechanical Engineering and Materials Science Zhong, Zhanwei; Duke University, Electrical and Computer Engineering Huang, Po-Hsun; Duke University, Mechanical Engineering and Material Sciences Katsanis, Nicholas; Duke University, Center for Human Disease Modeling Chakrabarty, Krish; Duke University, Electrical and Computer Engineering Huang, Tony; Duke University, Mechanical Engineering and Materials Science

Lab on a Chip

Paper

Contactless, programmable acoustofluidic manipulation of objects on water†

Received xxxth May 2019,
Accepted xxxth May 2019

DOI: 10.1039/x0xx00000x

www.rsc.org/

Peiran Zhang,[a] Chuyi Chen[a], Feng Guo,[b] Julien Philippe[c], Yuyang Gu,[a] Zhenhua Tian,[a] Hunter Bachman,[a] Liqiang Ren,[b] Shujie Yang,[a] Zhanwei Zhong,[d] Po-Hsun Huang,[a] Nicholas Katsanis,[c] Krishnendu Chakrabarty,[d] and Tony Jun Huang[a§]

Contact-free manipulation of small objects (e.g., cells, tissues, and droplets) using acoustic waves eliminates physical contact with structures and undesired surface adsorption. Pioneering acoustic-based, contact-free manipulation techniques (e.g., acoustic levitation) enable programmable manipulation but are limited by evaporation, bulky transducers, and inefficient acoustic coupling in air. Herein, we report an acoustofluidic mechanism for the contactless manipulation of small objects on water. A hollow-square-shaped interdigital transducer (IDT) is fabricated on lithium niobate ($LiNbO_3$), immersed in water and used as a sound source to generate acoustic waves and as a micropump to pump fluid in the ± *x* and ± *y* orthogonal directions. As a result, objects which float adjacent to the excited IDT can be pushed unidirectionally (horizontally) in ± *x* and ± *y* following the directed acoustic wave propagation. A fluidic processor was developed by patterning IDT units in a 6-by-6 array. We demonstrate contactless, programmable manipulation on water of oil droplets and Zebrafish larvae. This acoustofluidic-based manipulation opens avenues for the contactless, programmable processing of materials and small biosamples.

Introduction

Microfluidics has become an indispensable tool for modern biomedical research involving high-throughput screening,[1] rare cell separation,[2,3] and lab miniaturization and automation.[4] For example, digital microfluidics[5,6] can realize the programmable manipulation of small droplets using electrowetting or dielectrophoretic forces. However, it generally relies on physical contact with solid substrates for droplet actuation. Contact-free manipulation mechanisms (e.g., acoustics,[7] magnetics,[8] electrics,[9] surface tension[10]) eliminate the need for physical contact with solids, minimizing surface adsorption and avert mechanical impact on fragile samples (e.g., protein crystals).[11] The combination of microfluidics and acoustics provides versatile, contactless manipulation platforms based on acoustofluidics.[12,13] Various acoustofluidic functions, including particle translation (i.e., acoustic tweezers),[14-20] liquid handling (e.g., pumping, mixing, wetting), [21-25] model organism manipulation,[26,27] particle separation[28-31] and sorting,[32,33] have been realized. Recently, there has been growing interest in small-object manipulation in open space using acoustic waves due to its contactless operation, label-free nature, and high biocompatibility.[13] Acoustic levitation realizes contact-free object manipulation by suspending particles or droplets in air using standing bulk acoustic waves (BAWs)[7,11], and it has been developed into holographic[34-39] and digital[40,41] forms. This method provides unique advantages such as multipath routing without solid holders in open space, as well as the elimination of surface adsorption and associated contamination. However, the inefficient acoustic coupling in air, the rapid evaporation in air, and the bulky size of the transducers limit the manipulation of acoustic levitation on small objects. Acoustic hologram lenses[42] immersed in water offer higher resolution for object manipulation in water (i.e., mm-scale) but with pre-defined tracks, since the profile of the meta-surface is fixed after fabrication. To achieve contactless, programmable, and precise object manipulation, a straightforward strategy is to apply on-demand, local actuation forces on objects without direct contact.

Herein, we present an alternative mechanism for programmable, contactless manipulation of small objects via the combined effect of acoustic streaming and acoustic radiation forces. Acoustic streaming generates a unidirectional flow upon the gradient of time-averaged, acoustic momentum flux, and is generated accompanying acoustic attenuation.[43,44] As a proof-of-concept, floating micro-liter mineral oil droplets were tested. Our device is an array of hollow-square-shaped interdigital transducers (IDTs) on a lithium niobate ($LiNbO_3$) substrate embedded beneath a carrier water layer, which isolates the floating objects from the solid surfaces. Each IDT unit in the array can be excited independently to generate acoustic waves and the associated acoustic streaming in the water layer by applying resonant sinusoidal alternate current. Therefore, a floating microliter mineral oil droplet near the

[a] Department of Mechanical Engineering and Material Science, Duke University, NC 27708, USA.
[b] Department of Engineering Sciences and Mechanics, The Pennsylvania State University, PA, 16801, USA.
[c] Center for Human Disease Modeling, Duke University Medical Center, Durham, NC, 27701, USA.
[d] Department of Electrical and Computer Engineering, Duke University, NC, 27708, USA
§ Please address correspondence to Prof. Tony Jun Huang at tony.huang@duke.edu.
† Electronic Supplementary Information (ESI) available: xxx. See DOI: xxx.

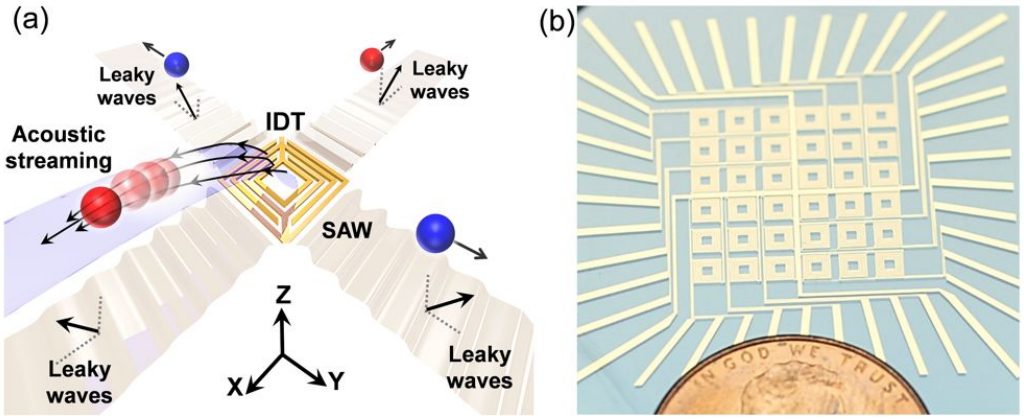

Figure 1. Contactless, programmable acoustofluidic manipulation of objects on water. (a) Schematic showing one unit of the acoustofluidic device. The oil droplets (red and blue spheres) are isolated in water to prevent direct contact with surfaces. This unit IDT has a hollow square structure and generates SAWs in ± *x* and ± *y* directions. The acoustic waves propagate, leak into the carrier liquid to form jets which propulse droplets along orthogonal axes on the surface of water. (b) Device image. The acoustofluidic chip consists of 36 pixels, each individually excitable.

excited IDT will be driven along the ±*x* or ±*y* orthogonal directions following the hydrodynamic gradients and the propagation directions of surface acoustic waves (SAW) in water. This device actuates droplets by pushing while confining them within unidirectional paths. This is instead of focusing objects to pressure nodes[40] or transporting objects via relayed hydrodynamic trapping wells, as demonstrated in previous acoustofluidic devices.[45,46] Using this method, we demonstrate contactless, programmable manipulation of oil droplets and Zebrafish larvae on water. This mechanism provides an alternative method for the contactless acoustic manipulation of materials and biosamples on water, and it will benefit applications involving emulsions, immiscible solvents, and biological samples.

Results

Acoustic wave propagation and acoustic streaming. As shown in Fig. 1a, a hollow-square-shaped IDT on a *Y*-128° cut $LiNbO_3$ substrate is employed for generating acoustic waves in the water layer. Once a resonant excitation signal is applied to the IDT, periodically distributed displacements will be generated over the arrays of metallic fingers via a piezoelectric effect. These local displacement distributions of IDT finger pairs propagate as SAWs. They are super-positioned and emitted through the IDT apertures as resonant vibrations of which correlate with the pitch distances. On one hand, an immersed IDT on the *Y*-128° $LiNbO_3$ substrate will generate SAWs and propagate along the surface of the $LiNbO_3$ substrate following the opening directions of two apertures. The SAWs propagate and couple into the water layer as leaky waves. On the other hand, besides SAW, local vibrations—transverse and oblique waves—also leak into the water layer. The contribution of both leaky waves creates four symmetric flow jets in 3D space in the water layer. As a result, the hollow square IDT pumps fluid out along the *x*-and *y*-axes and pumps in fluids along both diagonal directions in the top view. These fluid jets gradually extend to the surface of the water and form a three-dimensional hydrodynamic gradient that actuates the floating droplets on the surface of the water layer in four directions on the 2D plane. Therefore, an array consisting of 6 × 6 IDTs (Fig. 1b) can move the floating droplets on arbitrary routes by activating different unit IDTs adjacent to droplets. Different from a previously demonstrated digital acoustofluidics system[45] which uses a relayed hydrodynamic potential well to trap and transport droplets, in the current device the droplets adjacent to an excited IDT will be pushed unidirectionally on the surface of water along the directions of SAW propagation.

Fig. 2a and 2b schematically show the cross-sections of streamlines in the *x*-*z* and 45° *y*-rotated *x*-*z* planes. A symmetrical, 3D streaming pattern is established upon the activation of the IDT. The hollow-square-shaped IDT serves as a micro-pump that pumps fluid out following four horizontal directions of SAW propagation (*i.e.*, ± *x* and ± *y*) (Fig. 2a, 2c, 2d, and Fig. S1) and pumps in fluid along diagonal axes (Fig. 2b and Fig. 2e) to replenish fluids, which agrees with our simulation results as shown in Fig. 2f based on Supplementary Note S1 and Fig. S2.† The top view of a streaming pattern on the water's surface is shown in Fig. 2d. The 45° *y*-rotated *x*-*z* cross-sectional view is shown in Fig. 2e. Fig. 2g numerically demonstrates the propagation of the leaky waves in the water layer.

With a low attenuation coefficient of acoustic waves in water, the waves reaching the liquid surface still have considerable amplitude and impinge the interface. Therefore, beside moving the droplets, they also create a path well as a static 'ripple' (i.e., water-air interface deformation, Fig. S3) on the water's surface along the wave propagation direction.† The height of this 'ripple' is proportional to the incident pressure amplitude upon the balance between the 'ripple' gravity and acoustic radiation force.[47,48] Moreover, the reflected and incident waves form a standing wave in the loading fluid; this contains a pressure node near the surface.[47,48] A droplet positioned on a 'ripple' is constrained in a local minimum energy state within the path.[42] It moves along the direction of wave propagation upon the combination of acoustic radiation force

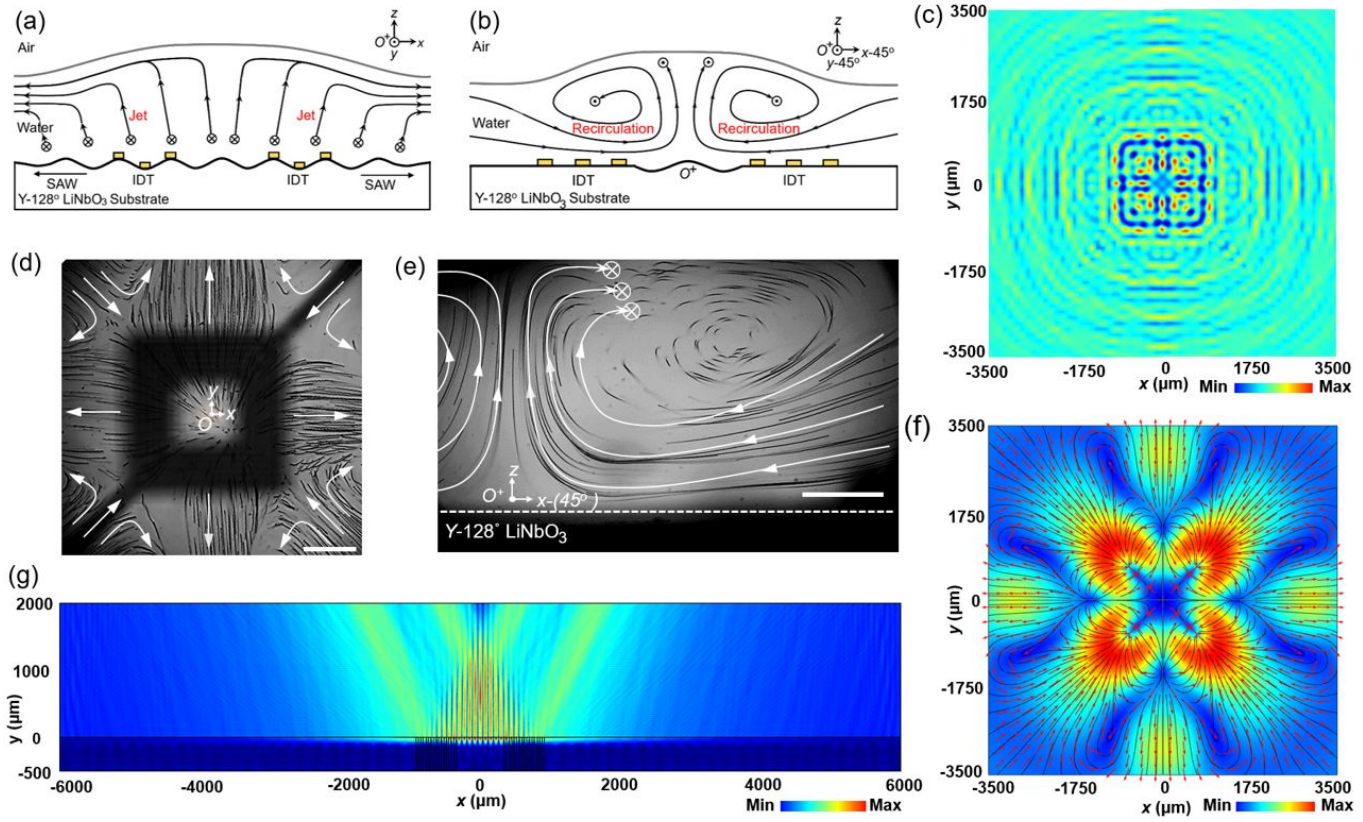

Figure 2. A streaming pattern generated upon the activation of IDTs. (a) Schematic *x*-*z*-plane cross-sectional view of the streaming pattern at an acoustic transducer (at $y = 0^+$). The origin (O) is located at the geometrical center of the hollow square transducer. The acoustic waves propagating around the water layer generated symmetrical fluid jets in ± *x* and ± *y* directions. Those fluid jets extend to the surface of water and push the floating oil droplets horizontally. (b) Schematic 45˚-rotated *x*-*z* cross-sectional view of the streaming pattern at the transducer (at $y\text{-}45^\circ = 0^+$). The circles with crosses indicate the tendency of flow going inside the display plane (i.e., the – *y*-45˚ direction). (c) Simulated acoustic pressure distribution in a fluid slice right above the IDT area. (d) Top view (*x*-*y*-plane, *z* = 2 mm) of stacked images of particle trajectories over an activated transducer. The focal plane is on the surface of the water. The transducer pumps fluid out along the *x*- and *y*-axes, and pumps fluid from the four corners of the transducer. The black hollow square is the IDT's image, which is out of focus. (e) 45˚-rotated *x*-*z* cross-sectional view (i.e., $y\text{-}45^\circ = 0^+$) of stacked images of particle trajectories. The white lines and arrows indicate the direction of streamlines. The circles with a cross indicate the tendency of flow going inside the displayed plane. 10-μm polystyrene particles show the streaming pattern in the focal plane. Scale bars: 800 μm. (f) Simulated x-y-plane (*z* = 2 mm) cross-sectional view of acoustic streaming velocity on the surface of the water. The liquid deformation is not considered in this model. (g) Simulated x-z-plane (*y* = 0 mm) cross-sectional view of absolute acoustic pressure distribution in the water layer over an excited IDT.

and acoustic streaming-induced hydrodynamic drag force, allowing the unidirectional droplet translation.

Droplet Actuation. The experimental droplet actuation process is shown in Fig. 3a and Fig. S4.† Once an IDT is activated (indicated by the white arrow), the droplet adjacent to the aperture of IDT first quickly accelerates and then moves to adjacent pixels (*i.e.*, independent IDTs) following the direction of wave propagation at a roughly constant speed (Fig. 3a). An immersed IDT unit can swiftly move droplets near its four apertures in ± *x* and ± *y* directions. The relationship between acoustic power and droplet actuation step time (*i.e.*, the travel time for a droplet to traverse 2.7 mm from unit to unit) is shown in Fig. 3b. The time for moving a droplet from unit to unit can be tuned from 1.2 s to 0.2 s by changing the power of the signal from 28 dBm to 37 dBm. The corresponding relationship of the traveling time for five unit-to-unit distances, as well as the displacement with different powers, are quantitatively illustrated in Fig. S5.† The particle tracking experiments show that the droplet moves approximately 4-fold faster than the flow on the water's surface (Fig. S6). This droplet moves 6.75 mm to the excited transducer, which suggests that the mixed effect of acoustic streaming and radiation force is the main mechanism for the unidirectional droplet translation.†

The droplet can also be actuated piecewise with a pulsed signal (Fig. 3c, Movies S1 and S2) to achieve precise displacement control.† The time-dependent speed change of both constant and pulsed (2 Hz, 20% duty ratio) propelling of droplets by a unit transducer is in Fig. S7.† The travelling speed of droplets will decrease dramatically when the viscosity of the carrier fluid is increased (*e.g.*, 40% glycerol solution) (Fig. S8).† Fig. S9 demonstrates the distance-dependent droplet travelling speed under a pulsed excitation signal (*i.e.*, 2 Hz, 20% duty ratio) with different carrier fluids (*i.e.*, water, 40 % glycerol water solution).†

As shown in Fig. S10 and Movie S3, two particle-containing oil droplets translated toward each other, then they merged per the "Cheerios effect."† Maintaining the droplet position depends on the viscosity of the carrier fluid (Movie S4); the

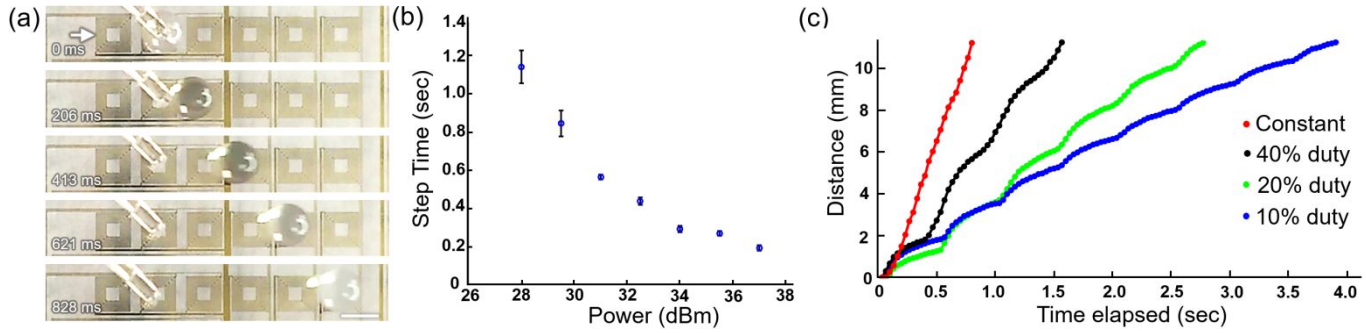

Figure 3. (a) Time-lapsed droplet trajectories at constant input power. The droplet is added manually via pipette. Power: 34 dBm. Frequency: 24 MHz. Scale bar: 2.5 mm. (b) A diagram showing the relationship between the excitation power and step time (*i.e.*, the travel time for a droplet traverse from unit to unit at a distance of 2.7 mm). (c) A diagram showing the relationships between the elapsed time and the traveling distance of a droplet in water upon the activation of the IDT using constant and pulsed input signals (*i.e.*, 2 Hz, 10%, 20%, and 40% duty ratios). The dots indicate the positions of the geometric center of a droplet with respect to the initial position. Dot-to-dot time interval: 34 ms. Power: 34 dBm. Frequency: 24.2 MHz.

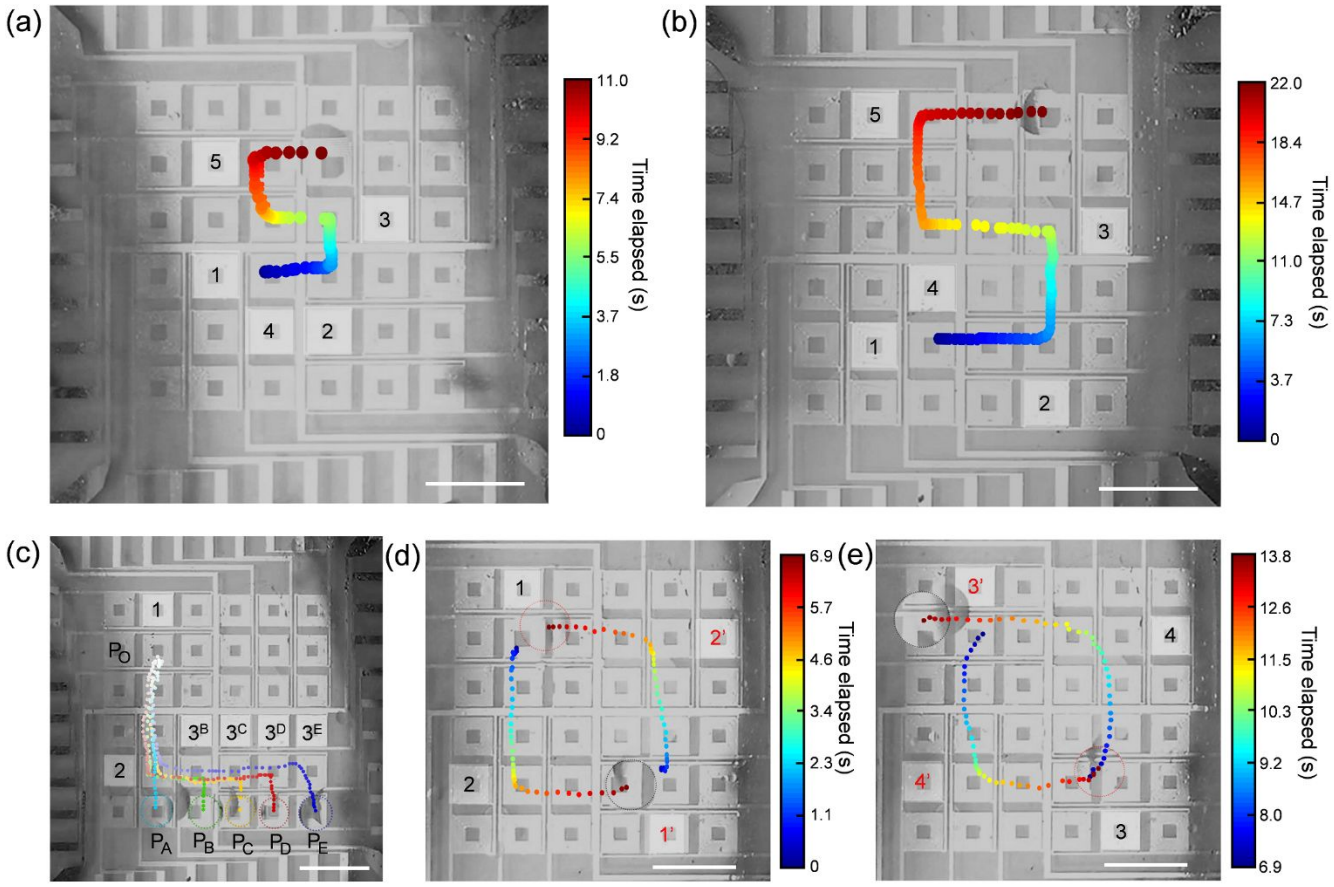

Figure 4. Programmable acoustic actuation of droplets. The time interval between dots was 180 ms. Power: 28 dBm. Frequency: 24.2 MHz. Scale bars: 5 mm. (a) Time-lapsed droplet trajectory for writing a small letter 's'. The color indicates the elapsed time. The activation sequences and corresponding positions of IDTs are indicated in colored numbers from 1 to 5. (b) Time-lapsed droplet trajectory writing a large letter 'S'. (c) Multiportal translation of droplets. The droplet was translated from pixels P_o to other pixels (P_A, P_B, P_C, P_D, and P_E) by following different activation sequences of IDT; these are indicated by numbers. The colored dots mark the positions of droplets on different routes (P_o – P_A: Cyan; P_o – P_B: Green; P_o – P_C: Yellow; P_o – P_D: Red; P_o – P_E: Blue). The interval between dots was 180 ms. A deeper color indicates a longer elapsed time. The dashed circle indicates the final positions of the droplets. (d) – (e) Parallel rotation of two droplets. (d) Droplet trajectory of the first half of the circle (0 – 6.9 s). The red circle and the black circle indicate the end positions of two specific droplets droplet in (a) and (b). The colored dots indicate the positions of droplets at specific times. Warmer colors are for longer elapsed times. The activation sequences and corresponding positions of IDTs are indicated in colored numbers from 1 to 4. The numbers with and without a prime sign (') indicate two independent IDT activation sequences. (e) Droplet trajectory of the second half of the circle (6.9 – 13.8 s).

droplet drifted with environmental air flow.† Alternatively, a droplet's position was maintained actively by exciting two opposing transducers (Fig. S11, Movie S5) or eight surrounding transducers (Fig. S12, Movie S6), where the viscous drag and acoustic radiation forces were balanced.†

Programmable Droplet Translation. By arranging the IDTs into a 6 × 6 array on a $LiNbO_3$ wafer, a programmable droplet processor with 36 independent pixels was developed. A droplet can thereby be translated in *x* and *y* directions from unit to unit along the hydrodynamic gradients triggered by adjacent transducers. By selectively activating the IDT units in a predetermined schedule, sophisticated routes can be realized. Fig. 4a shows an oil droplet translated on a trajectory of a small letter 's' by sequentially turning on and off 1 ~ 5 transducers. Similarly, there was a trajectory of a large 'S' (Fig. 4b, Movie S7); it has a translation distance twice as large as the small 's' for a single IDT.† As shown in Fig. 4c, by alternating the combination and sequences of IDT activation (1-2, 1-2-3^B, 1-2-3^C, 1-2-3^D, and 1-2-3^E), the droplet is translated from an initial position (port P_o) to different positions (P_A, P_B, P_C, P_D, and P_E) on the fluidic processor (Movie S8).† The time-serial trajectories of droplets on five different routes are indicated by colored dots, respectively. This function is critical for the multipath routing and sorting of free objects on a planar device. This also demonstrates good maneuverability with the device. Two droplets were used to demonstrate the parallel manipulation capability of our acoustofluidic droplet processor. We manually dispensed two mineral oil droplets at the initial positions, as indicated by blue dots in Fig. 4d. After we turned on the IDT units 1 and 1' at the same time, the droplets moved along the y-axis in opposite directions. After 4.1 s, units 2 and 2' were turned on, and the two droplets moved along the x-axis in opposite directions (Fig. 4d). The process was repeated after 6.9 s, resulting in two closed-loop trajectories (Fig. 4e, Movie S9).† The two droplets were synchronously rotated from 1 to 2 to 3 to 4 and 1' to 2' to 3' to 4'. Since the four outward fluid-jets generated by the immersed transducer extended across the transducer array (Fig. S13), spatiotemporal planning of the routing of droplets was needed to avoid interference between unit-transducers or collisions when actuating multiple objects.†

Contactless manipulation of Zebrafish larvae. Zebrafish (*Danio rerio*) have desirable attributes such as production of large numbers of externally fertilized eggs, and they have relatively small and transparent larvae with rapid organ formation. Zebrafish can be genetically manipulated, so there are many mutant and transgenic reports. About 70% of zebrafish genes have an identifiable human ortholog, which makes the zebrafish amenable to model human genetic disease and also makes this model organism relevant for high-throughput, small-molecule screening for drug treatment.[49] The development of an acoustic-based, biocompatible, contact-free manipulation mechanism will provide a unique alternative for zebrafish manipulation and the automation of drug screening within a compact device. In this work, we demonstrate the contactless manipulation of zebrafish larvae *via* acoustic streaming. The 5-day post-fertilization zebrafish larvae were anesthetized in 1× tricaine solution prior to loading to the device using a pipette. As shown in Fig. 5, the anesthetized zebrafish larvae were loaded at the apertures of two neighboring IDT units, as indicated by the red squares (1st-stage actuation). Because the larva had an irregular, spindle-like shape, two IDT units were used to ensure consistent actuation of the larvae. Upon the excitation of the two units, the zebrafish larvae were translated upward following the direction of SAW propagation, as indicated by the arrows. Once the larvae reached the opposite side of the array, the 1st-stage IDT units were turned off and the 2nd-stage IDT units (marked with blue squares) were turned on. With different configurations of IDT excitation, the selection of zebrafish larvae was realized by translating them to the left (Fig. 5a), middle (Fig. 5b), or right (Fig. 5c). The otic vesicles of the larvae are marked using dots to illustrate consistent tracking of their positions. Notably, the larvae were reoriented following the acoustic streaming with minimal hydrodynamic resistance, regardless of their initial orientations. The associated acoustic streaming pattern of the excitation of two adjacent transducers is shown in Fig. S14.† The acoustic streaming flow was tilted when the output of one transducer was significantly weaker than the other.

All data was acquired with the same zebrafish larva. After 50 repetitions of action during 1.5 hr experiments, the larva was recovered in egg water for 5 min and checked by microscope. The larva demonstrated normal mobility in the egg water and cardiac activity.

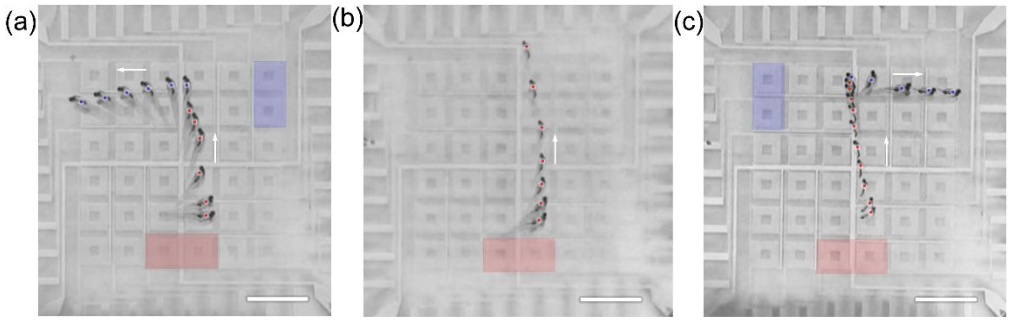

Figure 5. Acoustofluidic-based, contactless actuation and selection of a 5-day post-fertilization (dpf) zebrafish larvae. Red squares indicate the excited IDTs at the 1st stage. Blue squares indicate the excited IDTs at the 2nd stage. The zebrafish larva was moved to the left, middle, or right following the configurations of IDT excitation shown in (a), (b), or (c), respectively. The dots indicate the position of the larvae otic vesicles. The dot-to-dot interval was 400 ms. The arrows indicate the directions of larva translation. Power: 28 dBm. Frequency: 24.2 MHz. Scale bars: 5 mm.

Conclusion and Discussion

In this study, we demonstrated an acoustofluidic-based platform for the digital actuation of small objects on the surface of water. Mineral oil droplets and zebrafish larvae floating on the water surface were used as a proof-of-concept. Each of the unit IDTs in an array embedded beneath the carrier fluid served as a micro-pump for fluids along the *x*- and *y*-axes. Therefore, an object can be programmed to move in predesigned routes following the sequential triggering of hydrodynamic gradients by selectively switching different unit IDTs ON and OFF. In this work, we use the mixed effect of acoustic radiation and streaming in the water layer to push the floating object following the directions of SAW propagation.

Currently, the device is not energy-efficient due to the following issues. On one hand, the electro-mechanical coupling co-efficient is only ~0.05 for the Y-128 $LiNbO_3$ substrates. The electro-mechanical coupling co-efficient can be increased to 0.50 – 0.60 if one switches to other piezoelectric materials like lead zirconate titanate (PZT). On the other hand, the excitation signals being used should be considered as RF signals, although they can be as low as tens of MHz. This means to ensure maximal power efficiency, the transducer's design, switches, layout, and connections must be configured and optimized following the mature design principles of RF circuits; otherwise the energy applied cannot be efficiently utilized by the transducer due to the reflection, radiation, or heating effect of the signal. To address this issue, we are in a process of designing customized circuits to power and control the acoustofluidic devices.

Our acoustofluidic platform employs an immiscible carrier fluid for object actuation and does not use solid structures to contain samples. The elimination of a solid-liquid interface brings several advantages such as being free from surface-adsorptions and potentially detrimental mechanical impact on fragile samples (e.g., embryos, crystals). Additionally, this design enables water-immiscible, low-polarity droplets (e.g., organic solvents such as mineral oil, hexane) to be manipulated on our acoustofluidic devices. Comparing with electro-wetting based methods, more works are needed to address the following issues as the interferences between activated unit transducers (Fig. S12) and dynamic spatiotemporal planning.

In conclusion, this acoustofluidic mechanism enables programmable and contactless translation of small objects on the surface of water. It paves the way for the development of contact-free manipulation in various applications involving emulsions, tissues, or small animals in biology and chemistry.

Material and Methods

Device Fabrication. 5 nm Cr / 50 nm Au were deposited on a 128° Y-cut lithium niobate wafer (Precision Micro-Optics, USA) using an e-beam evaporator after standard photolithography. The hollow-square-shaped IDT array was rotated by 45° with respect to the *x*-axis of the single crystal wafer for uniform SAW speed, which meant the diagonal axis of the IDT was parallel to the *x*-axis of $LiNbO_3$. Silver epoxy (MG Chemicals, USA) bonded 32-gauge wires to our acoustofluidic chip. The dimensions of the hollow square transducer were 1.8375 mm for the outer length and 0.7125 mm for the inner length. The pitch distance between pixels was 0.8625 mm.

Device operation. A network analyzer was used to determine the optimal device operating frequency prior to operation, because it varied from device to device due to manual error during fabrication. The typical working frequency was 24 - 24.2 MHz. The chip was immersed in 2 mm-thick DI water and powered by a sinusoidal AC signal from a function generator (DG 3102C, Teletronics Technology Corporation, PA, USA) and an amplifier (25A250A, Amplifier Research, USA). 1 µL mineral oil droplet was dispensed with a pipette to a designated position on the surface of the water. The unit transducers were connected and disconnected manually to move droplets.

Reagents. Mineral oil was purchased from Sigma-Aldrich Corp. (Oakville, ON, USA). Tricaine (MS-222) was also purchased from Sigma-Aldrich, and it was made at 20× (4g/L ethyl 3-aminobenzoate methanesulfonate salt, pH adjusted to 7.4 with 1 M Tris) and used at 1× prior to anesthetization. Blue polystyrene particles (BLPMS 0.85 – 1.00 mm) were purchased from Cospheric LLC., USA.

Data processing. Videos were decomposed into frames and analyzed with ImageJ (National Institutes of Health, USA). Derived positions were plotted with MATLAB 2016a (Mathworks, MA, USA); the code is available from the corresponding authors upon request.

Particle tracking. 10-µm polystyrene particles (density: 1.05 g/cm^3, Bangs Lab Inc., USA) were used to streamline characterization. The video was recorded with a fast camera (Mini AX200, Photron Inc., USA). For the particle-tracking experiments at 45° rotational view, the transducer was placed perpendicular to the bottom surface of the liquid container on a microscope. The focal plane was chosen to be coincident with the geometric center of the IDT by tuning the fine scale on the *z*-axis knob. The derived high-speed video was decomposed and stacked with ImageJ to illustrate the streamlines.

Zebrafish Husbandry. All zebrafish experiments were conducted with approval from the Duke University Institutional Animal Care and Use Committee (IACUC). All experiments were performed in compliance with the relevant laws and institutional guidelines at Duke University (USA). All embryos were obtained from natural mating of wild-type adult fish (ZDR strain). Embryos were raised at 28.5 °C in egg water (0.3 g/L NaCl, 75 mg/L CaSO4, 37.5 mg/L NaHC03, 0.003% methylene blue) until five days post-fertilization (dpf).

Conflicts of interest

There are no conflicts to declare in this manuscript.

Acknowledgements

We acknowledge support from the National Institutes of Health (R01GM132603, R33CA223908, and R01GM127714), United States Army Medical Research Acquisition Activity (W81XWH-18-1-0242), and National Science Foundation (ECCS-1807601). We also acknowledge support from the Shared Materials Instrumentation Facility (SMIF) at Duke University.

Author Contributions

P.Z., F.G., L.R., and T.J.H. designed the research; P.Z., J.P., S.Y. performed the research; C.C. did the simulation; P.Z., C.C., Y.G., and Z.T. analyzed the data; P.Z., C.C., Z.Z., P.H., H.B., J.P., N.K., K.C. and T.J.H wrote the paper.

References

1 Y. C. Tung, A. Y. Hsiao, S. G. Allen, Y. S. Torisawa, M. Ho and S. Takayama, *Analyst*, 2011, **136**, 473-478.
2 H. W. Hou, M. E. Warkiani, B. L. Khoo, Z. R. Li, R. A. Soo, D. S. W. Tan, W. T. Lim, J. Han, A. A. S. Bhagat and C. T. Lim, *Sci. Rep.*, 2013, **3**, 1259.
3 H. Tsutsui, and C. M., Ho, *Mech. Res. Commun.*, 2009, **36**, 92-103.
4 T. Thorsen, S. J. Maerkl and S. R. Quake, *Science*, 2002, **298**, 580-584.
5 V. Srinivasan, V.K. Pamula and R. B. Fair, *Lab Chip*, 2004, **4**, 310-315.

6 J. Lee, H. Moon, J. Fowler, T. Schoellhammer and C.J. Kim, *Sens. Actuators, A*, 2002, **95**, 259-268.
7 E. H. Trinh, *Rev. Sci. Instrum.*, 1985, **56**, 2059-2065.
8 M. K. Khaw, C. H. Ooi, F. Mohd-Yasin, R. Vadivelu, J. St John and N. T. Nguyen, *Lab Chip*, 2016, **16**, 2211-2218.
9 O. D. Velev, B. G. Prevoand and K. H. Bhatt, *Nature*, 2003, **426**, 515.
10 A. S. Basu and Y. B. Gianchandani, *J. Microelectromech. Syst.*, 2009, **18**, 1163-1172.
11 S. K. Chung and E. H. Trinh, *J. Cryst. Growth*, 1998, **194**, 384-397.
12 L. Y. Yeo and J. R. Friend, *Annu. Rev. Fluid Mech.*, 2014, **46**, 379-406.
13 A. Ozcelik, J. Rufo, F. Guo, Y. Gu, P. Li, J. Lata, and T. J. Huang , *Nat. Methods,* 2018, **15**, 1021-1028.
14 Z. Tian, S. Yang, P. H. Huang, Z. Wang, P. Zhang, Y. Gu, H. Bachman, C. Chen, M. Wu, Y. Xie and T. J. Huang, *Sci. Adv.*, 2019, **5**, 6062.
15 D. J. Collins, C. Devendran, Z. Ma, J. W. Ng, A. Neild and Y. Ai, *Sci. Adv.*, 2016, **2**, 1600089.
16 J. P. Armstrong, S. A. Maynard, I. J. Pence, A. C. Franklin, B. W. Drinkwater and M. M. Stevens, *Lab Chip*, 2019, **19**, 562-573.
17 P. Glynne-Jones, C. E. Demore, C. Ye, Y. Qiu, S. Cochran and M. Hill, IEEE Trans. *Ultrason. Eng.*, 2012, **59**, 1258-1266.
18 H. Bruus, *Lab Chip*, 2012, **12**, 1014-1021.
19 S. M. Naseer, A. Manbachi,M. Samandari,P. Walch,Y. Gao, Y. S. Zhang, F. Davoudi, W. Wang, K. Abrinia, J.M. Cooper and A. Khademhosseini, *Biofabrication*, 2017, **9**, 015020.
20 G. Destgeer, J. H. Jung, J. Park, H. Ahmed, K. Park, R. Ahmad and H. J. Sung, *RSC Adv.*, 2017, **7**, 22524-22530.
21 P. H. Huang, N. Nama, Z. Mao, P. Li, J. Rufo, Y. Chen, Y. Xie, C. H. Wei, L. Wang and T. J. Huang, *Lab Chip*, 2014 **14**, 4319-4323.
22 L. Schmid, A. Wixforth, D. A. Weitz and T. Franke, *Microfluid. Nanofluid.*, 2012, **12**, 229-235.
23 R. Shilton, M. K. Tan, L. Y. Yeo and J. R. Friend, *J. Appl. Phys.*, 2008, **104**, 014910.
24 A. R. Rezk, O. Manor, J. R. Friend and L. Y. Yeo, *Nat. Comm.*, 2012, **3**, 1167.
25 Z. Guttenberg, H. Müller, H. Habermüller, A. Geisbauer, J. Pipper, J. Felbel, M. Kielpinski, J. Scribaand A. Wixforth, *Lab Chip*, 2005, **5**, 308-317.
26 D. Ahmed, A. Ozcelik, N. Bojanala, N. Nama, A. Upadhyay, Y. Chen, W. Hanna-Rose and T. J. Huang, *Nat. Comm.*, 2016, **7**, 11085.
27 Z. Yang, K. L. Cole, Y. Qiu, I. M. Somorjai, P. Wijesinghe, J. Nylk, S. Cochran, G. C. Spalding, D. A. Lyons and K. Dholakia, *Nat. Comm.*, 2019, **10**, 669.
28 M. Wu, Y. Ouyang, Z. Wang, R. Zhang, P. H. Huang, C. Chen, H. Li, P. Li, D. Quinn, M. Dao, S. Suresh, Y. Sadovsky, and T. J. Huang, *Proc. Natl. Acad. Sci. U. S. A.*, 2017, **114**, 10584-10589.
29 C. W. Shields IV, L. M. Johnson, L. Gao and G. P. López, *Langmuir*, 2014, **30**, 3923-3927.
30 T. Laurell, F. Petersson, and A. Nilsson, *Chem. Soc. Rev.*, 2007, **36**, 492-506.
31 D. J. Collins, Z. Ma, J. Han and Y. Ai, *Lab Chip*, 2017, **17**, 91-103.
32 L. Ren, S. Yang, P. Zhang, Z. Qu, Z. Mao, P. H. Huang, Y. Chen, M. Wu, L. Wang, P. Li and T. J. Huang, *Small*, 2018, **14**, 1801996.
33 Z. Ma, Y. Zhou, D. J. Collins and Y. Ai, *Lab Chip*, 2017, **17**, 3176-3185.
34 O. Youssefi and E. D. Diller, *IEEE Robot. Autom. Lett.*, 2019.
35 A. Watanabe, K. Hasegawa and Y. Abe, *Sci. Rep.*, 2018, **8**, 10221.
36 M. A. Andrade, T. S. Camargo and A. Marzo, *Rev. Sci. Instrum.*, 2018, **89**, 125105.
37 A. Marzo and B. W. Drinkwater, *Proc. Natl. Acad. Sci. U. S. A.*, 2018, **116**, 84-89.
38 A. Marzo, S. A. Seah, B. W. Drinkwater, D. R. Sahoo, B. Long and S. Subramanian, *Nat. Comm.*, 2015, **6**, 8661.
39 P. Zhang, T. Li, J. Zhu, X. Zhu, S. Yang, Y. Wang, X. Yin and X. Zhang, *Nat. Commun.*, 2014, **5**, 4316.
40 D. Foresti, M. Nabavi, M. Klingauf, A. Ferrari and D. Poulikakos, *Proc. Natl. Acad. Sci. U. S. A.*, 2013, **110**, 12549-12554.
41 T. Vasileiou, D. Foresti, A. Bayram, D. Poulikakos and A. Ferrari, *Sci. Rep.*, 2016, **6**, 20023.
42 K. Melde, A. G. Mark, T. Qiu and P. Fischer, *Nature*, 2016, **537**, 518-522.
43 M. Wiklund, R. Green and M. Ohlin, *Lab Chip*, 2012, **12**, 2438-2451.
44 Y. Q. Fu, X. Y. Du, J. K. Luo, A. J. Flewitt, W. I. Milne, D. S. Lee, N. M. Park, S. Maeng, S. H. Kim, Y. J. Choi and J. Park, *Sensors*, 2007, 478-483.
45 S. P. Zhang, J. Lata, C. Chen, J. Mai, F. Guo, Z. Tian, L. Ren, Z. Mao, P. H. Huang, P. Li, S. Yang and T. J. Huang, *Nat. Comm.*, 2018, **9**, 2928.
46 C. Chen, S. P. Zhang, S. Z. Mao, N. Nama, Y. Gu, P. H. Huang, Y. Jing, X. Guo, F. Costanzo and T. J. Huang, *Lab Chip*, 2018, **18**, 3645-3654.
47 N., Bertin, H., Chraibi, R., Wunenburger, J. P., Delville and E., Brasselet, *Phys. Rev. Lett.*, 2012, **109**, 244304.
48 B. Issenmann, R. Wunenburger, H. Chraibi, M. Gandil and J. P. Delville, *J. Fluid Mech.*, 2011, **682**, 460-490.
49 C. A. MacRae and R. T., Peterson, Zebrafish as tools for drug discovery. *Nat. Rev. Drug Discovery*, 2015, **14**, 721.